Regular Article

Ultrafast formation of exciplex species in dicyanoanthracene ZSM-5 revealed by transient emission and vibrational spectroscopy

Lucie Duplouy[1], Matthieu Hureau[1], Aurélien Moncomble[1], Svetlana Mintova[2], Olivier Gardoll[3], Alain Moissette[1], and Vincent De Waele[1,a]

[1] UMR 8516, LASIRE-Laboratoire de Spectroscopie Pour Les Interactions, La Réactivité et L'Environnement, Univ. Lille, CNRS, 59000 Lille, France
[2] Laboratoire Catalyse et Spectrochimie (LCS) ENSICAEN, UNICAEN, CNRS, Normandie Université, 6 Boulevard Maréchal Juin, 14050 Caen, France
[3] UMR 8181, UCCS-Unité de Catalyse et Chimie du Solide, Univ. Lille, CNRS, Bât. C3, 59650 Villeneuve d'Ascq Cedex, France

Abstract The photo-physical properties of dicyanoanthracene (DCA) molecules adsorbed on the external surface of ZSM-5 zeolite, forming DCA@ZSM-5 composites, have been investigated by picosecond transient emission, femtosecond transient absorption infrared vibrational spectroscopy, steady-state UV–vis, and quantum chemistry calculations. Following the photoexcitation at 420 nm of DCA@ZSM-5, the formation of the localized, LE, excited S_1 state of DCA emitting below 500 nm is observed. LE is rapidly and quasi-exclusively converted into two distinct exciplex species, EX1 and EX2, detected by their emission above 520 nm, with a lifetime of 5 ns and 20 ns, respectively. The different transient species can be identified by the frequency of the CN stretching vibration that is a marker of the charge delocalisation and that is peaking respectively at 2162 (LE), 2174 (EX1) and 2187 (EX2) cm^{-1}. DFT and TD-DFT calculations further support the assignment. The results show that the external surface of zeolite is an appropriate playground for the development of novel photoactive host–guest materials.

1 Introduction

Owing to their remarkable architecture, constituting a regular porous 3D organization of cages and channels whose dimensions are comparable with the size of small chemical entities (molecules, metal complexes or nanoparticles), zeolites constitute a family of microporous materials that are very attractive to design photoactive supramolecular host–guest assemblies [1–6] and promising for applications in the fields of photocatalysis, non-linear optical and luminescent materials, solar cell, sensing, photochemistry, and environmental remediation. Not only the spatial organization in the void of the zeolite framework but also the effects of the confinement of guest compounds in the cages and channels result in novel photo-physical and photochemical behaviors [7–13] that find their root in the earliest fs-ps processes following the photoexcitation [11, 13–18]. Therefore, elucidating the photo-physical and photochemical processes governing these applications by ultrafast time-resolved spectroscopy contributes to the optimal and original development of these photoactive host–guest materials.

In most of the studies and applications, the guest chemical species are incorporated into the zeolite by adsorption onto the large internal surface of the porous structure. Beside this common approach, chemical species with dimensions larger than the diameter of the pores can be adsorbed on the external surface of the zeolite crystallites to modulate their photoactivity [19–22]. This alternative strategy for the development of photoactive materials is interesting notably due to the fact that larger molecular compounds can carry several photoactive groups to design multifunctional materials. While micro-sized zeolite crystals exhibit a rather small external surface area (10–50 m^2/g) in comparison to the internal surface are (ca 500

[a] e-mail: vincent.de-waele@univ-lille.fr (corresponding author)

2146

Eur. Phys. J. Spec. Top. (2023) 232:2145–2156

m^2/g), the emergence of zeolites synthesized in the form of nano-sized crystallites and films [23, 24] or of 2D-nanosheets [25] has significantly increased the surface-to-volume ratio and the transport efficiency of these materials. This opens novel possibilities for exploiting the high external surface of the zeolitic materials, also in synergy with the encapsulation of active guest compounds whose photochemical behavior can potentially be strongly modified as the dimension of the zeolite is approaching the unit-cell dimension [26, 27]. Among other properties, the zeolites are effective in controlling the charge separation between electron donor and acceptor systems [8, 28], in certain cases, the zeolite framework participates even directly to the process of charge stabilization [29–32]. The photo-transfer of electrons between the external surface and the internal surface of zeolite can also be achieved by adsorbing electrons donating and withdrawing compounds [33]. The control of the photo-separation of charge by zeolite is promising in view of photovoltaic, photo-electrochemical and photocatalytic applications.

In this context, we are interested in the spectroscopic characterization of the transient species formed in the fs-ps times scale by charge separation at the surface of the zeolites. In this work, we investigated the functionalization of the external surface of ZSM-5 zeolite microcrystallites by the adsorption of 9,10-dicyanoanthracene (DCA) molecules (Scheme 1). The penetration of DCA in the channel of the MFI structure of ZSM-5 is sterically hindered by the two cyano groups in para position of the central benzyl moiety. Nevertheless, the molecules of DCA can adsorb on the strong binding sites located at the pore opening which can interact by hydrogen bonding with the SiOH or by partial intercalation inside the channel of ZSM-5, or they can adsorb on weaker surface sites, by hydrogen bonding or Van der Waals interaction, and then they adopt different orientation [22].

The molecules of DCA exhibit an electron acceptor character in the S_1 excited state (E = 1.99 V_{NHE}) making them a strong photo-oxidizing species [34]. So, cyano-substituted arenes molecules are good model compounds to investigate the photoinduced charge separation [35–39] dynamics in solution. So far, the influence of the zeolite of the ultrafast charge separation photodynamics is still poorly documented. We addressed in this work the study of the photophysics of DCA molecules absorbed on ZSM-5, hereafter **DCA@ZSM-5.** We investigated specifically the nature of the excited states generated upon the photoexcitation of the solid **DCA@ZSM-5** by combining time-resolved emission spectroscopy (TCSPC) measurements and femtosecond transient absorption measurements with an IR probe. The later spectroscopy allowed us to follow the CN stretching vibration that is a good marker of the charge localization in cyano-aromatics molecules [40–45]. To the best of our knowledge, fs IR transient absorption was only applied to zeolite sample to investigate the OH stretching vibration of the framework hydroxyl surface group [46] or of adsorbed water [47] and methanol [48] molecules. With

the advances of this spectroscopy, the sensitivity allows us to envision more complex guest compound as it will be illustrated in the following. Quantum chemical calculations are completing the experimental results and interpretation.

2 Experimental

2.1 Material preparation

DCA@ZSM-5 samples were prepared according a well-established procedure [31, 32]. NaZSM-5 samples (Si/Al $\sim$ 13.5; average particle size 1 µm) were obtained from VAW aluminum (Schwandorf, Germany). 9,10-dicyanoanthtacene (DCA, $C_{16}H_{12}N_2$ 97% Sigma-Aldrich) was purified by sublimation. Potassium bromide (KBr $\geq$ 99% Sigma-Aldrich) was used for pelletization. Pure and dry Ar gas was used to keep our samples under inert atmosphere.

1.2 g of the NaZSM-5 zeolite was weighted and introduced into a long tube-shaped evacuable and heatable silica cell. The tube was then placed in a vertical oven connected to a gas piping network and heated stepwise up to 450 °C under dry argon for at least 12 h. The sample was then cooled down to room temperature and kept under dry argon flow. The zeolite was transferred into a sealed silica cell connected to dry Ar and vacuum pipes. Weighted amounts of DCA at the concentration DCA:ZSM-5 20 mg/g (9×10^{-5} mol of DCA per gram) were added into the cell without any solvent, the whole set-up being kept under dry Ar. The powders were shaken until the resulting mixture was homogeneous and transferred under dry Ar in a sealed quartz glass Suprasil cell. The sample was placed into an oven kept at 40 °C for the sorption to take place via sublimation. For the subsequent analyses, the sample was kept in the cell or pelletized with KBr.

2.2 Thermogravimetric measurements

The moisture content and the organic compound (9,10-dicyanoanthtacene, $C_{16}H_{12}N_2$) were investigated using a SETSYS (SETARAM) analyzer (heating rate of 5 °C min^{-1} under 40 mL min^{-1} flow of air).

2.3 Steady-state diffuse reflectance and emission spectroscopy.

A Cary 6000 spectrophotometer was used to record the UV–visible absorption spectra between 200 and 1800 nm. An integrating sphere was connected to the spectrophotometer to measure the diffuse reflectance from the powdered samples stored under dry argon in the Suprasil cells; the corresponding dehydrated bare zeolite was taken as the reference. The Kubelka–Munk
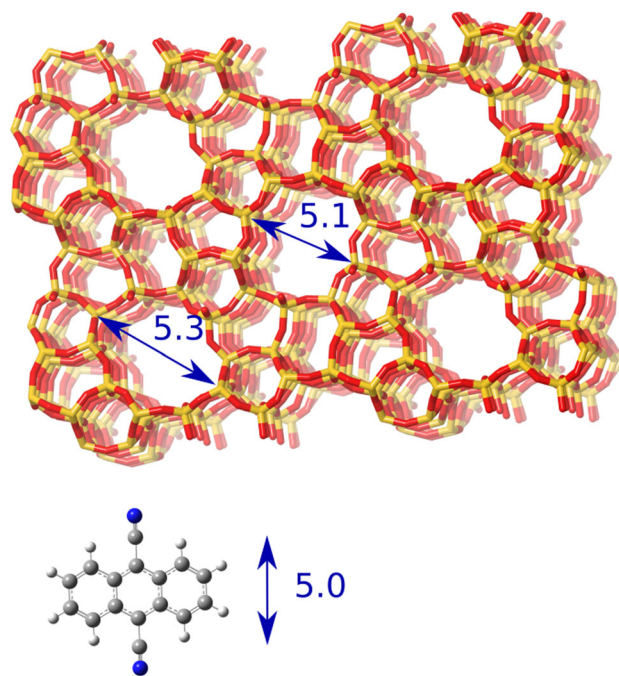
Scheme 1 Scheme of the MFI framework of the ZSM-5 zeolite along the (010) channel and molecule structure of the 9,10-dicyanoanthracene for comparison. The lengths are given in Angstroms

function was used to plot the DR UV–vis spectra:

$$F(R) = \frac{(1-R)^2}{2R}$$

R is the ratio of the diffuse reflectance of the loaded zeolite and bare one. $F(R)$ is a function of wavelength.

A Horiba Fluorolog-3 spectrofluorimeter was used to record the emission spectra between 450 and 800 nm. The apparatus was set in the front face mode to allow the measure of the powdered sample sealed in the quartz cell and in the right-angle mode to measure the emission from the pelletized samples.

2.4 Steady-state vibrational spectroscopy

An Avatar 360 spectrometer (Thermo Nicolet) equipped with a DTGS detector (400–4000 cm^{-1}) was used to record in transmission the infrared spectra with a resolution of 0.5 cm^{-1}. The Raman spectra were recorded using a FT Raman spectrometer (Bruker RFS 100/S instrument) with a laser excitation at 1064 nm.

2.5 Time-correlated single-photon counting measurements

The fluorescence decays were measured using the TCSPC spectroscopy using the set-up described here [49]. Briefly, the 420 nm excitation pulses were generated by a femtosecond Ti:sapphire laser (Coherent Chameleon Ultra II, 80 MHz, 200 fs, 3.8 W) coupled

with a pulse picker (4 MHz) and a harmonic generator (SHG/THG, APE). The fluorescence lifetime measurements were carried out with the FT200 PicoQuant spectrometer and the emission signal was collected with a polarizer set at the magic-angle and a Czerny-Turner type monochromator connected to a computer for observation wavelength selection. The photons were collected with a cooled microchannel plate photomultiplier tube R3809U (Hamamatsu) and recorded using a PicoHarp 300 TCSPC system (PicoQuant). The instrumental response function (IRF) was measured using Ludox, a colloidal silica and the full width at half maximum (FWHM) was found to be $\sim$ 50 ps. For these experiments, the **DCA@ZSM-5** pellets were mounted on a dedicated home-made support and the emission was collected at ca. 45 degrees. The excitation was cut using a color filter. The software used to plot and process the decays was FluoFit v.4.6.6 (PicoQuant) and a home-made Python script.

2.6 IR femtosecond transient absorption measurements

The pump-probe femtosecond transient absorption set-up is based on Ti:Sa CPA laser (Coherent Libra HE 4 W) delivering at 1 kHz, short pulses with a duration of 100 fs and a wavelength centered at 800 nm. 1.4 mW is used to generate the pump beam by SHG, FHG, or SFG in a UV–vis OPA (Coherent OPERA). 2.4 mW is seeded in a second Mid-IR OPA equipped with a NDFG stage to generate the probe beam in the Mid-IR spectral range (3–20 μm). For these experiments, the pump laser beam was set at 420 nm. After the OPA stage,

the pump beam is stirred using high reflective dielectric mirrors to the entrance of an optical delay line, passing through a Berek waveplate (New Focus) and neutral density filters to adjust the polarization and the intensity of the pump excitation. The optical delay line consists of an aluminum retroreflector mounted on a motorized translation stage (Newport Delay line + controller). After the delay line, the pump beam is propagated and slightly focused several millimeters in front of the surface of the sample by mean of a CaF_2 lens (typically $f = + 300$ mm). The wavelength of the probe beam was centered at 4.65μm, which allow us to record the IR spectra between 2250–2050 cm^{-1}. After generation, the probe beam is propagated through a fixed optical delay line made of gold stirring planar mirrors and 2 off-axis (15°, f = + 600 mm) parabolic mirrors that have been aligned to collimate the beam with a ca. 1 magnification. This optical path is compensating the time delay between the output of the pump and probe OPAs. Then the probe beam is focused into the sample by an off-axis parabolic mirror (30°, $f = + 450$ mm). The reference (REF) and signal (SIG) beam are generated by inserting a 4 mm thick BaF_2 window (Thuet) on the optical path of the IR probe beam, between the focusing parabolic mirror and the sample. The sample is placed at the foci of REF and SIG that are vertically distant by 3–4 mm. After the sample, SIG and REF are imaged on the entrance slit of a spectrograph (Horiba iHr320) and detected by a LN2-cooled MCT 2*32 pixels arrays detector (IR-3216, Infrared Systems development). The intensity of each individual SIG and REF pulse is recorded and stored. An optical chopper at 500 Hz synchronous of the laser pulse is placed on the pump beam and its state is recorded by the IR-3216 simultaneously to the SIG and REF signal.

For this study, the transient spectra have been typically recorded by carrying out 3–4 scans of the pump-probe delays, with an average of 3000–5000 pulses per step. REF and SIG beam were dispersed using a 300 gr/mm grating ($\lambda_{\text{blaze}} = 6 \mu$m), resulting in a spectral resolution of 1–2 cm^{-1}/px. Under these conditions, we reconstructed the transient spectra covering the spectral range 2240–2120 cm^{-1} by the concatenation of three or four independent spectral acquisitions. The transient IR response of the DCA is superposed to a broad and featureless component that was subtracted from each spectrum (see SI).

The femtosecond transient absorption spectra are recorded in transmission by dispersing the sample (**DCA@ZSM-5**) in a 100 mg KBR pellet. The amount of **DCA@ZSM-5** was adjusted to limit the scattering and absorption of the IR probe radiation by the zeolite in the 2000–2500 cm^{-1} spectral window. For the fs IR measurements, the samples are placed in a homemade optical cell composed by a LN2-colled cryostat mounted on a XYZ translation stage and a vacuum chamber coupled to a turbo pump and a gas delivering systems. The pellet is located in the middle of the chamber, about 5 cm away from the two 1 mm thick BaF_2 windows of the cell. Two samples can be hold in

the compartment for a better control and reproducibility of the pump-probe measurements under the in situ conditions. In this study, all the measurements were performed at room temperature under vacuum. The pellets were dehydrated in the cell at 10^{-6} mbar for several hours before each experiment.

## 2.7 Quantum chemistry calculations

All the computations were carried out using the Gaussian 16 suite of programs. [50] Energies were computed in the framework of Density Functional Theory (DFT). The PBE0 global hybrid functional [51, 52] was used throughout with an empirical dispersion correction (GD3). [53] The underlying wave function was developed on the aug-CC-PVTZ basis set [54] on all atoms. Geometries were fully optimized in the vacuum using standard algorithms. The nature of the stationary points was checked by vibrational analysis that also yields the harmonic frequencies that are reported without any scaling in this publication.

3 Results and Discussion

3.1 Absorption of DCA at the surface of the ZSM-5 crystals

The structures of the ZSM-5 zeolite and of the DCA molecule are illustrated in Scheme 2. From the characteristic length of the DCA molecule in comparison with the pore diameter of the ZSM-5 zeolite, it is quite obvious that DCA cannot freely enter and diffuse into the zeolitic channel. Therefore, the molecules of DCA are exclusively adsorbed on the external surface of the ZSM-5 crystals and at the mouth of the pores. This does not mean that there is no specific interaction with the zeolite surface and notably a partial inclusion of the molecule at the entrance of the channel, eventually facilitated by an expected vibrational bending of the CCN angle [22].

Figure 1 shows the TG and dTG curves obtained for **ZSM-5** and **DCA@ZSM-5** samples. For **ZSM-5**, the total weight lost is 5.1% and corresponds to the loss of the surface and occluded water molecules that occur below 400 °C. For **DCA@ZSM-5**, we notice two clear effects. First, a net increase of the percentage weight loss (+ 2%) in agreement with the amount of DCA deposited in the zeolite. Second, a net shift of the desorption temperature to a lower value indicating that the distribution of the water molecule is also perturbed in presence of DCA. This point is in good agreement with the fact that the aromatic compounds interact preferentially with the hydrophilic sites of the zeolite surface [22]. Therefore, we can conclude based on the thermogravimetric measurement that the crystals of ZSM-5 are in interaction with the DCA molecules predominantly on their external surface but also at the mouth of the pores. For a better understanding

Eur. Phys. J. Spec. Top. (2023) 232:2145–2156

2149
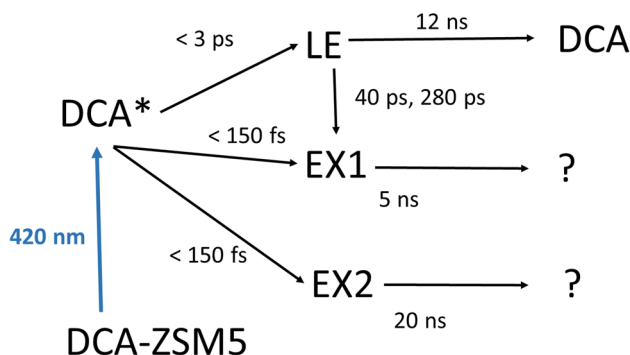
Scheme 2 Photo-physical processes involved following the photoexcitation of DCA@ZSM-5 at 420 nm

of DCA at the surface of ZSM-5, **Table 1** provides an estimation of the relevant parameters characterizing the **DCA@ZSM-5** composites. The pores at the entrance of the channels of the zeolite crystals constitute a favorable site of adsorption of DCA. From our assessment of the number of pore entrances at the surface of the crystallites, we estimated that ca. 25% of the DCA molecules can be accommodated, for example, in a configuration with one of the terminal benzene ring pointing inside the channel that represents a significant amount of the total of the DCA molecules. The rest of the DCA molecules will be spatially arranged on the external surface according to the specific interaction with zeolite surface and with the DCA molecules that are partially adsorbed in the pores. Advanced structural and textural analysis would be necessary to understand precisely the microscopic interaction of DCA with the MFI porous structure. Nevertheless, the characterization of the adsorption of DCA using the thermogravimetric analysis has provided the evidence of the interaction of the DCA molecules and the zeolite crystals. In the rest of the manuscript, we will focus on the photo-physical properties of **DCA@ZSM-5**, without any assumption regarding the hypothetic microscopic organization of the molecules at the surface of the zeolite.

3.2 UV–vis absorption and emission spectroscopy

The absorption and emission spectra ($\lambda_{exc} = 420$ nm) of **DCA@ZSM-5** are depicted in Fig. 2. The absorption spectrum of **DCA@ZSM-5** exhibits the typical vibronic progression of anthracene-like molecules which is composed of 3 peaks (marked 0-n, n = 1–3, on the graph) at 22,083 cm^{-1}, 23,535 cm^{-1}, and 25,308 cm^{-1}). Compared with the free molecule of **DCA** in solution [55], the 0–1 band is found at a lower energy. A similar effect, assigned to dipolar interactions in molecular crystal, was also reported for anthracene crystals and nanoaggregates [56]. The emission is also structured and exhibits three maxima observed at 20,033 cm^{-1}, peak a (499 nm), 18,333 cm^{-1}, peak b (546 nm), and 17,567 cm^{-1}, peak c (570 nm). In comparison with the free DCA molecules in solution [57, 58], we can notice
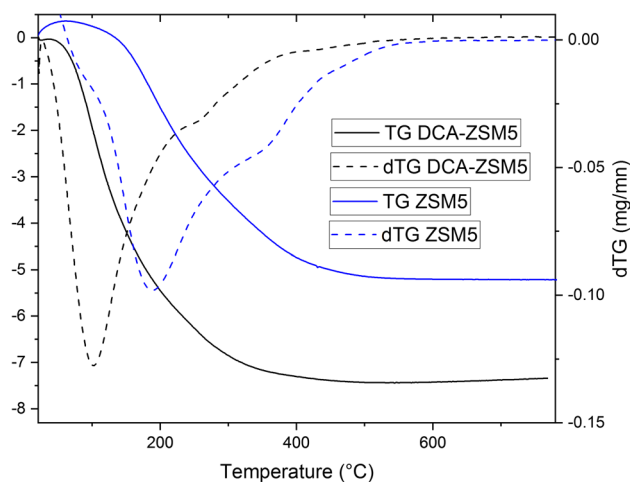

Fig. 1 TG (full line) and dTG (dash line) curved of **ZSM-5** (blue) and **DCA@ZSM-5** (black)

Table 1 Main properties of the DCA@ZSM-5 composite

ZSM-5	
Dimensions of the crystals (μm)	$2.2 \times 0.6 \times 0.5$
External surface, S_{ext} (m^2/g)[a]	10
Pores density, N_{pores} (/g)[b]	15×10^{18}
Pores surface, S_{pores} (m^2/g)[c]	3.75
DCA	
Concentration (molecules/g)	54×10^{18}
Surface equivalent S_{DCA} (m^2/g)[d]	54

[a] assuming the ZSM-5 density of 720 g/L,
[b] with 5 pores per 330 $Å^2$
[c] with a pore section of ca. 25 $Å^2$
[d] molecular surface of ca. 100 $Å^2$

in Fig. 2 that the emission spectrum is not the mirror of the absorption spectrum. Thus, the absorption and emission in Fig. 2 show that the DCA molecules in **DCA@ZSM-5** are in interaction with their neighbors in the solid state [56].
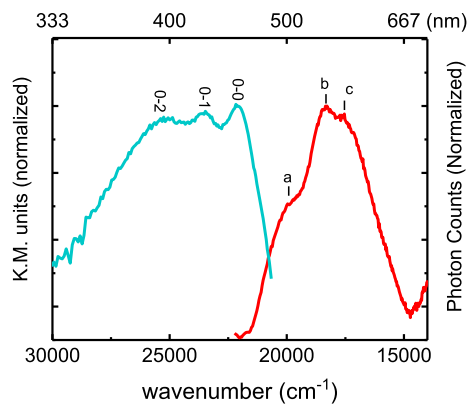
2150

Eur. Phys. J. Spec. Top. (2023) 232:2145–2156

Fig. 2 Absorption in Kubelka–Munk unit, and emission spectra ($\lambda_{exc} = 420$ nm) and **DCA@ZSM-5**

The luminescence of **DCA@ZSM-5** was characterized by time-resolved emission spectroscopy. The transient emission spectra reconstructed from the TCSPC emission decays are reported in Fig. 3. The temporal evolution of the emission of **DCA@ZSM-5** consists in two main contributions. First, a broad emission band, with a maximum located at 480–500 nm and a second maximum around 540 nm, is formed within the IRF of the set-up. During the first hundred of picosecond, the blue part of the emission is decreasing while a new
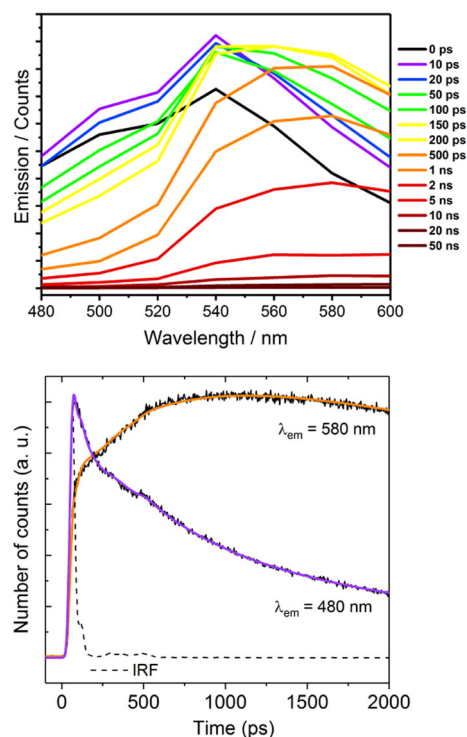

Fig. 3 (top) Transient emission spectra of **DCA@ZSM-5** reconstructed from the emission decays recorded by TCSPC upon photoexcitation at 420 nm, and (bottom) emission decay traces and their corresponding fit at 480 nm (violet) and 580 nm (orange). (–) is the IRF trace

broad contribution is growing above 550 nm. We notice the presence of a quasi-isosbestic point at 540 nm. After 500 ps, the emission spectrum is dominated by that second broad contribution which decays from 500 ps to 50 ns. For anthracene-like molecule, the emission in the blue part (< 500 nm) is associated with a localized S_1 state (**LE**), while the red-shifted contribution usually corresponds to the emission from exciplex species (**EX**). So, the temporal evolution of the emission spectra of **DCA@ZSM-5** can be described as (i) below 500 ps, the conversion between the locally excited state (**LE**) of the **DCA** molecules ($\lambda_{em} = 500$ nm) into an excimer species (**EX**) responsible for the long-lived emission above 540 nm, respectively, and (ii) the decay of the **EX** band in the ns time, whose maximum is shifting from ca 550 nm to 570 nm, suggesting the formation of different **EX** species, with different degrees of charge delocalization [55, 59, 60].

The decay of fluorescence recorded at 480 nm and 580 nm for **DCA@ZSM-5** are depicted in Fig. 3 (between 0 and 2 ns), and as supplementary information (full decay between 0 and 50 ns). The traces were fitted using a sum of four exponential decays functions (Table 2). At 480 nm, the signal appears within the IRF and the kinetic trace is well reproduced by a sum of two decays in the sub-ns regime (50 ps and 618 ps) totalizing 72% of the contribution and two decays in the ns timescale: 2.5 ns contributing to 22–24% of the decay, and a less important contribution (5–6%) equal to 13 ns. At 580 ns, about 65% of the signal appears within the IRF and this initial step is followed by rising component ($t'_2 = 567$ ps) that accounts for 33% of the total of the decay components. The time constants $t'_1 = 14$ ps and $t'_2 = 567$ ps for $\lambda_{em} = 580$ nm in Table 2 are in a reasonable agreement with their corresponding decays times at $\lambda_{em} = 480$ nm ($t_1 = 50$ ps and $t_2 = 618$ ps), and notably t_2 and t'_2 which are associated with a decreasing and increasing contribution, at $\lambda_{em} = 480$ nm and $\lambda_{em} = 580$ nm, respectively. We can also notice that the amplitude of the growth of the emission at 580 nm, associated with the time t'_2, only accounts for 33% of the total emission decay at this wavelength. Therefore, a fraction of the emitting state at $\lambda_{em} = 580$ nm is generated within the duration of the IRF. It corresponds therefore either to the excited state emitting at 480 nm or to a second **EX** species with a maximum around 540–550 nm. This second hypothesis is more convincing as it is also suggested by the shape of the spectra in Fig. 3. After the growing stage, the emission detected at 580 nm exhibits a main contribution with a lifetime of $t'_3 = 5.7$–5.9 ns and an additional longer decay time ($t'_4 = 21$–23 ns) accounting for 17–20% of the emission decay amplitude. These values are quite different from those measured at 480 nm so we ruled out the contribution of the **LE** state above 540 nm, and assume instead the formation of two distinct **EX** species.

In the following, the decay times (t_1, t_2, t_3, t_4) and (t'_1, t'_2, t'_3, t'_4), refer to the fit values at $\lambda_{em} = 480$ nm and $\lambda_{em} = 580$ nm, respectively. As the decay time $t_4 = 13$ ns is close to the emission lifetime of the molecule

Eur. Phys. J. Spec. Top. (2023) 232:2145–2156

2151

Table 2 Fit parameters of the emission decays of **DCA@ZSM-5** recording upon photo-excitation at 420 nm

λ_{em}	$t_1{}^a(a1)^b$	t_2 (a2)	t_3 (a3)	t_4 (a4)
480 nm	50 (34%)	618 (38%)	2.50 (22%)	13.1 (6%)
580 nm	14 (14%)	567 (− 33%)	5.75 (66%)	21.4 (20%)

[a] t_1, t_2, t_3,t_4 decay time obtained using a 4-exp model convolved by the IRF signal
[b] amplitude of the component of the fit given in percentage relatively to the total of the decaying components (i.e., positive amplitude). With this convention, the growth contributions appear with a negative percentage

of DCA in solution [38, 57], it is therefore assigned to decay of the S_1 (**LE**) state of DCA molecules in weak interaction with their surroundings, either spatially isolated or in a geometrical configuration unfavorable to the interaction with the surrounding molecules. This contribution has a small weight (6%), but it counts for more than 50% of the steady-state emission at this wavelength. The decays time $t_2 \approx t'_2 \approx 600$ ps is observed at both wavelength with an inverted amplitude sign and it corresponds to a conversion of the **LE** state of DCA into an excimer (**EX**) species**.** If we further assume that for these molecules of DCA in **DCA@ZSM-5**, the **LE** to **EX** conversion is in competition with the internal conversion by emission that is characterized by $t = 13$ ns for the non-interacting DCA, it comes out that 95% of the **LE** state is quenched to form the **EX** species. Therefore, we deduce from the amplitude of the different emission components that the number of photoexcited DCA that is converted into **EX** species is ca. 4 times more important than the ones decaying mainly by emission. Concerning the slow decaying processes at 580 nm, t'_3 and t'_4 are in good agreement with the reported lifetime for DCA or anthracene exciplexes, and the difference between the two values is assigned to different degrees of charge transfer [61]. The remaining short decays t_1, t'_1 and t_2 are similar to those reported for anthracene nanoaggregates [56] and they are assigned to the dynamics of the **LE** state whose lifetime is shortened by trapping at the surface and defect of the crystals. In **DCA@ZSM-5**, the adsorption of DCA molecules at the surface of zeolite favors the formation of defect and so, it supports this interpretation. Alternatively, the shortest t_1 and t'_1 components might also correspond to an ultrafast internal relaxation of **LE**.

3.3 Steady-state and transient vibrational properties of DCA@ZSM-5

In order to get a better insight of the nature of the **LE** and **EX** molecular configurations in **DCA@ZSM-5** we carried out femtosecond pump-probe MidIR spectroscopy and we focused on the CN stretching modes which is a good probe of the charge distribution in the cyano-molecular compounds. Complementary, quantum chemistry modeling of DCA ground state (S_0), lowest excited states (S_1, T_1) and DCA anion (DCA^-) have been performed to support the vibrational assignment.

3.3.1 Quantum chemical calculations

The electronic and vibrational properties of the molecule of DCA in the ground state (S_0), lowest excited singlet (S_1) and Triplet (T_1) state, and in the anionic form (DCA^-) have been calculated using the DFT and TD-DFT method, for the ground and excited state respectively. The corresponding HOMO and LUMO orbitals for the DCA in its ground state are reported in the Table 3. The lowest $S_1 \leftarrow S_0$ electronic transition is described at 98% by the HOMO and LUMO orbitals. From the representation of the orbitals in Table 3, we can clearly deduce the $\pi\pi^*$ nature of this electronic transition without a significant perturbation of CN bonds. So, in DCA, the electronic density on the CN bonds is only perturbed indirectly via the quinoïdal distortion of the central aromatic ring and the subsequent polarization of the carbon atoms in positions 9 and 10.

The vibrational normal modes and the corresponding wavenumbers and IR intensities were computed at the optimized geometry for the different species of DCA. The values for the symmetric and anti-symmetric CN elongation mode are reported in Table 4. From the theoretical modeling, for all the DCA species, only two normal modes are calculated with a frequency in the range 2000 -2400 cm^{-1} and they correspond to the symmetric and anti-symmetric combination of the CN stretching elongation, hereafter $\nu(CN)$. As expected, only the anti-symmetric mode is IR active, but the calculation also revealed the strong variation of the IR dipole moment, *i.e.,* of the intensity of the IR band, between these different chemical species, in good agreement with experimental investigations of nitriles anions [43]. The calculated value for $\nu(CN)$ also varies significantly with the nature of the DCA species and it is decreasing on going
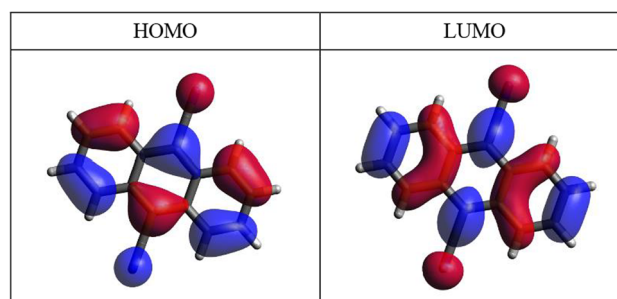
Table 3 HOMO–LUMO DCA molecular orbitals

HOMO	LUMO

2152

Eur. Phys. J. Spec. Top. (2023) 232:2145–2156

Table 4 Computed and observed values of the CN stretching vibration of DCA species

	S_0		S_1		T_1	Anion	
	Calc[a]	Obs	Calc	Obs	Calc	Calc	Obs
$\nu(CN)_{asym}$	2347	2213/2222[b]	2301	2160[d]	2257	2262	2216[e]
$\Delta\nu$[c]			− 46	− 57	− 90	− 85	− 99
Calc. μ_{IR}	79.2		146.0		30.0	721.9	
$\nu(CN)_{sym}$	2348	2217[b]	2301		2258		

[a] The calculated frequencies are unscaled.

[b] IR and Raman spectra (Fig. 4).

[c] observed and calculated shift relative to the value in S_0

[d] this work.

[e] Frequency for 9-cyanoanthracene from ref [43]

Fig. 4 a FTIR **b** Raman and **c** time-resolved IR spectra (λ_{pump} = 420 nm) of **DCA@ZSM-5** recorded in the region of the CN stretching mode
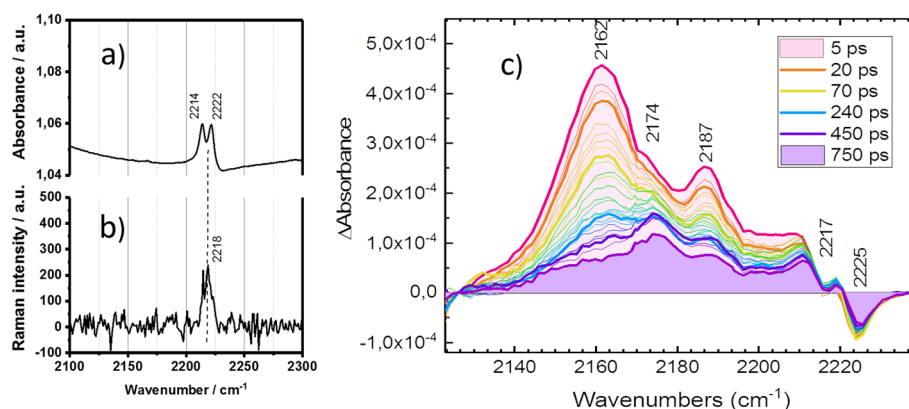
from the ground to the excited and then anionic states. The calculated variation of $\nu(CN)$ relative to the value in the ground S_0 are − 46 cm^{-1} (S_1), − 90 cm^{-1} (T_1) and − 99 cm^{-1} (DCA$^-$), respectively. As expected, the uncorrected harmonic DFT calculation overestimates the experimental frequencies but for a better agreement not only a scaling factor but also the anharmonicity must be included in the model [62]. This is out of the scope of the work. However, we can notice that the experimental shift of the CN frequency on going from the ground to the S_1 and to the anion species of DCA are well reproduced by the calculations (Table 4).

The IR and Raman vibrational spectra of **DCA@ZSM-5** in the spectra range of the CN stretch mode are depicted in Fig. 4. The frequencies are close to that measured for the molecule of DCA (see SI) showing that the structure of the DCA molecules is preserved in **DCA@ZSM-5** and that in the ground state no charge delocalization between the molecules or between the DCA and the zeolite surface occurs. The Raman spectrum exhibits a single vibrational band peaking at 2217 cm^{-1}, corresponding to the symmetric CN stretching mode that is Raman active by symmetry. The IR spectrum shows a doublet of vibrational bands instead of the single IR allowed transition of the anti-symmetric CN stretching modes. This feature is explained by a Fermi resonance the CN stretching mode with a combination of lower frequency vibration of DCA [63].

3.3.2 Time-resolved MidIR absorption spectroscopy

A set of transient spectra recorded for pump-probe delays up to 750 ps is depicted in Fig. 4. The transient IR spectrum recorded at 5 ps exhibits between 2120 and 2240 cm^{-1} two negative contributions (peaking at 2217 and 2225 cm^{-1}) and corresponding to the expected bleach signal of the ground state S_0 of DCA. A large and structured positive contribution extending from 2220 cm^{-1} to roughly 2120 cm^{-1} dominates the transient spectrum on which we can clearly identify two vibrational bands peaking at 2162 cm^{-1} and 2187 cm^{-1}, respectively, and a shoulder at 2174 cm^{-1}. The broad and intense band at 2162 cm^{-1} is assigned to the anti-symmetric stretching mode of the CN elongations of the S_1 state of DCA, hereafter $\nu_1(CN)$. This assignment is based on the CN stretching mode reported for the S_1 state of cyanoanthracene (CNA) [42] and it is also supported by the DFT and TDDFT calculations in Table 1 predicting a decrease of the wavenumber of $\nu_{as}(CN)$ of $\Delta\nu = 47$ cm^{-1}, in good agreement with the experimental data ($\Delta\nu = -57$ cm^{-1}) on going from the ground (S_0) and to lowest (S_1) excited state of DCA. We also point out that the calculations reveal the increase of the IR intensity of $\nu_{as}(CN)$ that is in good agreement with the experimental observation that the amplitude of the absorption band peaking at 2162 cm^{-1} is much higher than the negative contribution (bleach of the S_0 IR bands) in the transient spectra (Fig. 4). In addition to the band $\nu_1(CN)$ at

2162 cm^{-1} of the S$_1$ state of DCA, two additional vibrational bands are observed at 2174 cm^{-1} (ν_2(CN)) and at 2188 cm^{-1} (ν_3(CN)) suggesting the formation of two additional species exhibiting different electron distributions on the CN bonds. According to the calculations (Table 4) these bands cannot be associated with the T$_1$ state or with the anion of DCA. The frequency of these two bands is moreover not compatible with the hypothesis of hot vibrational states of the ground state of DCA [64]. Therefore, we assigned these two contributions to the formation of bound ion pair (**IP**) or exciplexes (**EX**) species of DCA molecules. Formally the difference between **IP** and **EX** resides only in the degree of charge delocalization. For CNA and tetracyanoethylene in solution, **EX/IP** states have been identified by their vibrational spectral signature in the 2150–220 cm^{-1} range [41, 42], that is between the S$_0$ and S$_1$ CN stretching frequency. In solution, the **EX** contribution is usually broad and featureless due to the delocalization of the electronic cloud over the two partner molecules and to the loose dynamical configuration in solution. **IP** pair gives rise to more defined bands.

For **DCA@ZSM-5**, between 5 and 500 ps the relative intensity of the three IR bands is evolving significantly (Fig. 4). The band ν_1(CN) $= 2162$ cm^{-1} is the most intense at short time but has nearly completely vanished after 250 ps. The intensity of ν_3(CN) $= 2187$ cm^{-1} is also decreasing but in much less proportion in comparison with ν_1(CN). In opposite, from 5 to 750 ps, the third band ν_2(CN) $= 2174$ cm^{-1} is becoming the most intense of the spectra, without significantly diminishing its amplitude. These different evolutions confirm the formation of three different transient chemical species. Figure 5 shows kinetic traces recording around $\Delta t = 0$. At negative delay, we can recognize the perturbed free induction decay contribution that was first described by P. Hamm [65] predicting the oscillatory component and the signal growth at the bleach wavenumber (2224 cm^{-1}). Besides, we can notice that the species associated with ν_3(CN) $= 2187$ cm^{-1} is formed within the pump-probe cross-correlation, while for ν_1(CN) $= 2162$ cm^{-1} the rise time is followed by a second step of growth up to 3 ps. The ground state bleach contribution (2224 cm^{-1}) does not evolve significantly, nor at short time or at long time (Fig. 4) showing that the internal conversion to the ground S$_0$ state is a minor process in the sub-ns time scale. Transient spectra recorded before 5 ps are given in Fig. 5. At this time scale, the slow growth of ν_1(CN) and the quasi-instantaneous formation of ν_2(CN) and ν_3(CN) are well resolved. The kinetic of the three CN vibration bands was fitted using 3 exponential decay times (SI and Table 5). The decay time $t_1 = 1.5$–1.8 ps is associated with the increase of the intensity of the band ν_1(CN). The same time constant t_1 and t_2 (40 ps) are obtained for ν_1(CN) and ν_2(CN), but it is because of the strong contribution of ν_1(CN) that dominates the fit. The longer decay time t_3 is equal to 282 ps and 393 ps, for ν_1(CN) and ν_2(CN), respectively, and it allows us to distinguish the two kinetics and to assign these two bands to two different species. For ν_3(CN) the

fit parameters reflect the formation of the band within the duration of our pulse-probe cross-correlation followed by a decay with the kinetic that mimics the decay of ν_1(CN) suggesting a correlation between these two bands. As at 750 ps the intensity of ν_1(CN) is less than that of ν_3(CN). We assume therefore that a partial conversion of the species associated with ν_1(CN), **LE**, into the species **EX** species associated with ν_3(CN) takes place. We notice also that the values of t_2 and t_3 are in good agreement with the emission lifetime measured by TCSPC (Table 1).

a) the amplitudes have been multiplied by 10^4.

From the analysis of the transient emission and vibrational spectroscopy data, the following mechanism (Scheme 2) can therefore be proposed for the photophysical behavior of **DCA@ZSM-5**:

– The first transient species that is formed upon photoexcitation is the localized excited S$_1$ state (**LE**) of the DCA molecules. **LE** can be clearly identified by its emission band below 500 nm, and the vibrational CN stretching mode ν_1(CN) peaking at 2162 cm^{-1}. Our data show that the **LE** state in **DCA@ZSM-5** is similar to the S$_1$ state of DCA molecules in solution. The lifetime of **LE** is however strongly reduced in **DCA@ZSM-5** and it decays following a bimodal distribution ($t_1 = $ ca. 40 ps, $t_2 = $ ca. 300 ps) resulting from the heterogeneity of the molecular arrangement and of structural defaults. We proved that **LE** is however not decaying by internal conversion to the ground state (S$_0 \leftarrow$ S$_1$), but it is converted efficiently into exciplex **EX** (or bounded ion-pair **IP**) species by the charge delocalization over one or several DCA entities.

– The formation of **EX** (**IP**) species is demonstrated by the emission spectra and the transient IR data. The highest time resolution of the latest spectroscopy allowed us to show that **EX** species are not only formed by conversion from the **LE**, but also directly (less than 100 fs) by charge transfer excitation. We clearly identified two **EX** species emitting above 520 nm and that can be differentiated by the frequency of the CN stretching vibration, respectively peaking at 2174 and 2188 cm^{-1}. These charge delocalized states have a lifetime of several nanoseconds that is also probably modulated by the microheterogeneity of the supramolecular organization.

Table 5 Fit parameters of the three main vibrational absorption bands

	ν_1(CN), 2162 cm^{-1}	ν_2(CN), 2174 cm^{-1}	ν_3(CN), 2187 cm^{-1}
t_1 (a_1)	1.5 ± 0.2 ps (-2.9)a)	1.8 ± 1.2 ps (-0.45)	0.2 ± 0.5 ps (0.36)
t_2 (a_2)	40 ± 10 ps (1.9)	43 ± 30 ps (0.48)	36 ± 11 ps (0.76)
t_3 (a_3)	282 ± 86 ps (2.17)	393 ± 97 ps (0.93)	309 ± 64 ps (0.94)

Fig. 5 Kinetic traces reconstructed from the transient spectra of **DCA@ZSM-5** and selected transient spectra for $\cdot t < 5$ ps ($\lambda_{\text{pump}} = 420$ nm)
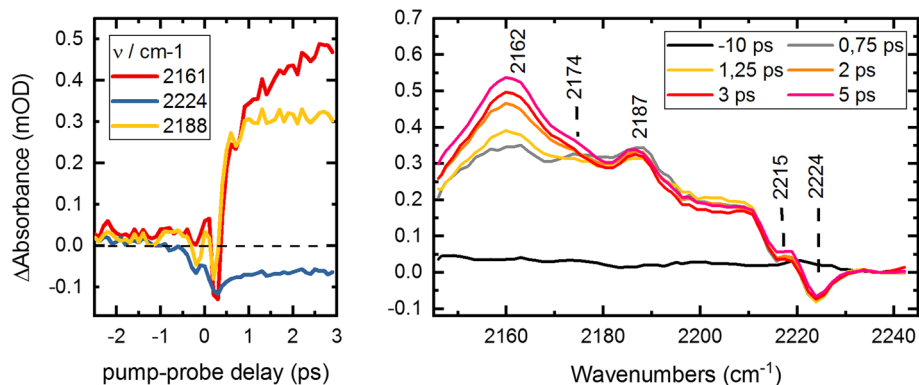
4 Conclusion

We have characterized by time-resolved spectroscopy (ps TCSCP emission and fs IR transient absorption) the transient chemical species that are generated upon the photoexcitation of DCA molecules adsorbed as dense layers at the surface of microcrystals of zeolite ZSM-5. Following the photoexcitation, the main mechanism is the ultrafast formation of charge delocalized species directly by resonance with a charge transfer transition, or within a few hundreds of picoseconds, through the formation of the localized (**LE**) S_1 state of DCA. Our results show the potential of **DCA@ZSM-5** for stabilizing efficiently and with a high yield of formation of charge separated states. Further investigations are necessary by carrying out similar photo-physical measurements at different degrees of dispersion of the DCA molecules at the surface, by modulating the molecular concentration but also the zeolite type and composition, for a more precise identification of the transient species and the role of the zeolites on their equilibrium and lifetime. Quantum chemistry could also provide a microscopic insight of the **EX** species.

From the spectroscopic point of view, this work has extended to the case of zeolites the application of the MidIR transient absorption spectroscopy to characterize photoinduced charge separation processes. We reported IR transient spectra of good quality and, more important, obtained at a reasonable guest concentration of 0.5 molecule/ u.c. So, under these spectroscopic conditions, it is fully possible to consider the investigation of molecules adsorbed at lower concentration, notably using zeolitic material exhibiting high external surface area like nanozeolites or nanosheets.

Data availability statement The data will be made available on reasonable request.

References

1. J.C. Scaiano, H. García, Intrazeolite photochemistry: toward supramolecular control of molecular photochemistry. Acc. Chem. Res. **32**, 783 (1999)
2. N.J. Turro, From boiling stones to smart crystals: supramolecular and magnetic isotope control of radical-radical reactions in zeolites. Acc. Chem. Res. **33**, 637 (2000)
3. G. Calzaferri, K. Lutkouskaya, Mimicking the antenna system of green plants. Photochem. Photobiol. Sci. **7**, 879 (2008)
4. H.S. Kim, K.B. Yoon, Preparation and characterization of CdS and PbS Quantum Dots in Zeolite Y and Their Applications for Nonlinear Optical Materials and Solar Cell. Coord. Chem. Rev. **263**–**264**, 239 (2014)
5. V. Ramamurthy, J. Sivaguru, Supramolecular Photochemistry as a Potential Synthetic Tool: Photocycloaddition. Chem. Rev. **116**, 9914 (2016)

6. O. Fenwick et al., Tuning the energetics and tailoring the optical properties of silver clusters confined in zeolites. Nat. Mater. **15**, 1017 (2016)

7. V. Ramamurthy, N.J. Turro, Photochemistry of organic molecules within zeolites: role of cations. J. Incl. Phenom. Mol. Recognit. Chem. **21**, 239 (1995)

8. S. Hashimoto, Zeolite photochemistry: impact of zeolites on photochemistry and feedback from photochemistry to zeolite science. J. Photochem. Photobiol. C Photochem. Rev. **4**, 19 (2003)

9. P.K. Dutta, Y. Kim, Photochemical processes in zeolites: new developments. Curr. Opin. Solid State Mater. Sci. **7**, 483 (2003)

10. M. Busby, C. Blum, M. Tibben, S. Fibikar, G. Calzaferri, V. Subramaniam, L. De Cola, Time, space, and spectrally resolved studies on j-aggregate interactions in Zeolite L nanochannels. J. Am. Chem. Soc. **130**, 10970 (2008)

11. S. Mintova, V. De Waele, M. Hölzl, U. Schmidhammer, B. Mihailova, E. Riedle, T. Bein, Photochemistry of 2-(2′-hydroxyphenyl)benzothiazole encapsulated in nanosized zeolites. J. Phys. Chem. A **108**, 10640 (2004)

12. R.Q. Albuquerque, J. Kühni, P. Belser, L. de Cola, On the reversible photoisomerization of spiropyran-modified zeolite l single crystals. ChemPhysChem **11**, 575 (2010)

13. N. Alarcos, B. Cohen, M. Ziółek, A. Douhal, Photochemistry and photophysics in silica-based materials: ultrafast and single molecule spectroscopy observation. Chem. Rev. **117**, 13639 (2017)

14. G. Flachenecker, A. Materny, The elementary steps of the photodissociation and recombination reactions of iodine molecules enclosed in cages and channels of zeolite crystals: a femtosecond time-resolved study of the geometry effect. J. Chem. Phys. **120**, 5674 (2004)

15. M. Gil, M. Ziółek, J.A. Organero, A. Douhal, Confined fast and ultrafast dynamics of a photochromic proton-transfer dye within a zeolite nanocage. J. Phys. Chem. C **114**, 9554 (2010)

16. T. Bein, Host-guest interactions in Zeolites and periodic mesoporous materials. Stud. Surf. Sci. Catal. **168**, 611–657 (2007)

17. M. Bryckaert, A. Kharchenko, O. Lebedev, B. Dong, I. De Waele, G. Buntinx, O. Poizat, S. Mintova, V. De Waele, Hot-electron photodynamics of silver-containing nanosized zeolite films revealed by transient absorption spectroscopy. J. Phys. Chem. C **121**, 26958 (2017)

18. F. Kawtharani, S. Mintova, R. Retoux, M. Mostafavi, G. Buntinx, V. De Waele, Hot-electron photodynamics in silver-containing BEA-type nanozeolite studied by femtosecond transient absorption spectroscopy. ChemPhysChem **21**, 2634 (2020)

19. J.K. Thomas, Physical aspects of photochemistry and radiation chemistry of molecules adsorbed on SiO2, γ-Al2O3, zeolites, and clays. Chem. Rev. **93**, 301 (1993)

20. J.K. Thomas, Physical aspects of radiation-induced processes on SiO2, γ-Al2O3, zeolites, and clays. Chem. Rev. **105**, 1683 (2005)

21. N.J. Turro, X.-G. Lei, W. Li, Z. Liu, A. McDermott, M.F. Ottaviani, L. Abrams, Photochemical and magnetic resonance investigations of the supramolecular structure and dynamics of molecules and reactive radicals on the external and internal surface of MFI zeolites. J. Am. Chem. Soc. **122**, 11649 (2000)

22. A. Moscatelli, Z. Liu, X. Lei, J. Dyer, L. Abrams, M.F. Ottaviani, N.J. Turro, Photolysis of Dibenzyl Ketones Sorbed on MFI zeolites in the presence of spectator molecules: cage effects, kinetics, and external surface sites characterization. J. Am. Chem. Soc. **130**, 11344 (2008)

23. V. Valtchev, L. Tosheva, Porous nanosized particles: preparation, properties, and applications. Chem. Rev. **113**, 6734 (2013)

24. S. Mintova, M. Jaber, V. Valtchev, Nanosized microporous crystals: emerging applications. Chem. Soc. Rev. **44**, 7207 (2015)

25. P. Kumar et al., One-dimensional intergrowths in two-dimensional zeolite nanosheets and their effect on ultra-selective transport. Nat. Mater. **19**, 443 (2020)

26. M. Hureau, A. Moissette, L. Tzanis, T.J. Daou, Effects of the zeolite particle size on the charge separated states. Microporous Mesoporous Mater. **254**, 121 (2017)

27. L. Duplouy, A. Moissette, M. Hureau, V. De Waele, T.J. Daou, I. Batonneau-Gener, Effect of zeolite morphology on charge separated states: ZSM-5-type nanocrystals, nanosheets and nanosponges. Phys. Chem. Chem. Phys. **22**, 12015 (2020)

28. Y. Kim, A. Das, H. Zhang, P.K. Dutta, Zeolite membrane-based artificial photosynthetic assembly for long-lived charge separation. J. Phys. Chem. B **109**, 6929 (2005)

29. X. Liu, J.K. Thomas, Photophysical properties of pyrene in zeolites: adsorption and distribution of pyrene molecules on the surfaces of Zeolite L and mordenite. Chem. Mater. **6**, 2303 (1994)

30. X. Liu, G. Zhang, J.K. Thomas, Spectroscopic studies of electron and hole trapping in zeolites: formation of hydrated electrons and hydroxyl radicals. J. Phys. Chem. B **101**, 2182 (1997)

31. A. Moissette, H. Vezin, I. Gener, J. Patarin, C. Brémard, Electron-hole pairs stabilized in Al-ZSM-5 Zeolites. Angew. Chem. - Int. Ed. **41**, 1241 (2002)

32. A. Moissette, S. Marquis, D. Cornu, H. Vezin, C. Brémard, Long-lived spin-correlated pairs generated by photolysis of naphthalene occluded in non-brønsted acidic ZSM-5 zeolites. J. Am. Chem. Soc. **127**, 15417 (2005)

33. P.K. Dutta, M. Severance, Photoelectron transfer in zeolite cages and its relevance to solar energy conversion. J. Phys. Chem. Lett. **2**, 467 (2011)

34. C. Yang, J.-D. Yang, Y.-H. Li, X. Li, J.-P. Cheng, 9,10-Dicyanoanthracene catalyzed decarboxylative alkynylation of carboxylic acids under visible-light irradiation. J. Org. Chem. **81**, 12357 (2016)

35. E. Vauthey, Investigation of the photoinduced electron transfer reaction between 9,10-dicyanoanthracene and 1-methylnaphthalene in acetonitrile using picosecond transient grating spectroscopy. J. Phys. Chem. A **101**, 1635 (1997)

36. E. Vauthey, C. Högemann, X. Allonas, Direct investigation of the dynamics of charge recombination following the fluorescence quenching of 9,10-dicyanoanthracene by various electron donors in acetonitrile. J. Phys. Chem. A **102**, 7362 (1998)

2156

Eur. Phys. J. Spec. Top. (2023) 232:2145–2156

37. S. Iwai, S. Murata, R. Katoh, M. Tachiya, K. Kikuchi, Y. Takahashi, Ultrafast charge separation and exciplex formation induced by strong interaction between electron donor and acceptor at short distances. J. Chem. Phys. **112**, 7111 (2000)

38. Y. Wang, O. Haze, J.P. Dinnocenzo, S. Farid, R.S. Farid, I.R. Gould, Bonded exciplexes. A new concept in photochemical reactions. J. Org. Chem. **72**, 6970 (2007)

39. E. Vauthey, Elucidating the mechanism of bimolecular photoinduced electron transfer reactions. J. Phys. Chem. B **126**, 778 (2022)

40. B. Dereka, M. Koch, E. Vauthey, Looking at photoinduced charge transfer processes in the IR: answers to several long-standing questions. Acc. Chem. Res. **50**, 426 (2017)

41. M. Koch, G. Licari, E. Vauthey, Bimodal exciplex formation in bimolecular photoinduced electron transfer revealed by ultrafast time-resolved infrared absorption. J. Phys. Chem. B **119**, 11846 (2015)

42. M. Koch, R. Letrun, E. Vauthey, Exciplex formation in bimolecular photoinduced electron-transfer investigated by ultrafast time-resolved infrared spectroscopy. J. Am. Chem. Soc. **136**, 4066 (2014)

43. T. Mani, D.C. Grills, M.D. Newton, J.R. Miller, Electron LOCALIZATION OF ANIONS PROBED BY NITRILE VIBRATIOns. J. Am. Chem. Soc. **137**, 10979 (2015)

44. G. Lee, D. Kossowska, J. Lim, S. Kim, H. Han, K. Kwak, M. Cho, Cyanamide as an infrared reporter: comparison of vibrational properties between nitriles bonded to N and C atoms. J. Phys. Chem. B **122**, 4035 (2018)

45. S. Choi, J. Park, K. Kwak, M. Cho, Substituent effects on the vibrational properties of the CN stretch mode of aromatic nitriles: ir probes useful for time-resolved IR spectroscopy. Chem. - Asian J. **16**, 2626 (2021)

46. J. Kubota, M. Furuki, Y. Goto, J. Kondo, A. Wada, K. Domen, C. Hirose, Vibrational lifetimes of surface hydroxyl groups of zeolites by picosecond IR pulses. Chem. Phys. Lett. **204**, 273 (1993)

47. M. Kashitani et al., Transient absorption spectra of vibrationally excited OH/OD groups in mordenite zeolites: effect of Xe adsorption. J. Chem. Phys. **105**, 6665 (1996)

48. M. Bonn, H.J. Bakker, A.W. Kleyn, R.A. Van Santen, Dynamics of infrared photodissociation of methanol clusters in zeolites and in solution. J. Phys. Chem. **100**, 15301 (1996)

49. A. Ghose et al., Emission properties of oxyluciferin and its derivatives in water: revealing the nature of the emissive species in firefly bioluminescence. J. Phys. Chem. B **119**, 2638 (2015)

50. M. J. Frisch et al., *Gaussian˜16 Revision C.01*, (2016).

51. J.P. Perdew, K. Burke, M. Ernzerhof, Generalized Gradient Approximation Made Simple. Phys. Rev. Lett. **77**, 3865 (1996)

52. C. Adamo, V. Barone, Toward reliable density functional methods without adjustable parameters: the PBE0 model. J. Chem. Phys. **110**, 6158 (1999)

53. S. Grimme, J. Antony, S. Ehrlich, H. Krieg, A consistent and accurate ab initio parametrization of density functional dispersion correction (DFT-D) for the 94 elements H-Pu. J. Chem. Phys. **132**, 154104 (2010)

54. R.A. Kendall, T.H. Dunning, R.J. Harrison, Electron affinities of the first-row atoms revisited. Systematic basis sets and wave functions. J. Chem. Phys. **96**, 6796 (1992)

55. J. Eriksen, C.S. Foote, Electron-transfer fluorescence quenching and exciplexes of cyano-substituted anthracenes. J. Phys. Chem. **82**, 2659 (1978)

56. B. Manna, R. Ghosh, D.K. Palit, Exciton dynamics in anthracene nanoaggregates. J. Phys. Chem. C **119**, 10641 (2015)

57. A.F. Olea, D.R. Worrall, F. Wilkinson, S.L. Williams, A.A. Abdel-Shafi, Solvent effects on the photophysical properties of 9,10-dicyanoanthracene. Phys. Chem. Chem. Phys. **4**, 161 (2002)

58. J.S. Beckwith, A. Aster, E. Vauthey, The excited-state dynamics of the radical anions of cyanoanthracenes. Phys. Chem. Chem. Phys. **24**, 568 (2022)

59. I.R. Gould, R.H. Young, L.J. Mueller, S. Farid, A.C. Albrecht, Electronic structures of exciplexes and excited charge-transfer complexes. J. Am. Chem. Soc. **116**, 8188 (1994)

60. R.H. Young, A.M. Feinberg, J.P. Dinnocenzo, S. Farid, Transition from charge-transfer to largely locally excited exciplexes, from structureless to vibrationally structured emissions. Photochem. Photobiol. **91**, 624 (2015)

61. E. Dolotova, D. Dogadkin, I. Soboleva, M. Kuzmin, O. Nicolet, E. Vauthey, Lifetimes of partial charge transfer exciplexes of 9-cyanophenanthrene and 9-cyanoanthracene. Chem. Phys. Lett. **380**, 729 (2003)

62. F. Vazart, C. Latouche, P. Cimino, V. Barone, Accurate Infrared (IR) spectra for molecules containing the C≡N moiety by anharmonic computations with the double hybrid B2PLYP density functional. J. Chem. Theory Comput. **11**, 4364 (2015)

63. J.M. Rodgers, R.M. Abaskharon, B. Ding, J. Chen, W. Zhang, F. Gai, Fermi resonance as a means to determine the hydrogen-bonding status of two infrared probes. Phys. Chem. Chem. Phys. **19**, 16144 (2017)

64. P. Coulter, M.P. Grubb, D. Koyama, I.V. Sazanovich, G.M. Greetham, A.J. Orr-Ewing, Recombination, solvation and reaction of CN radicals following ultraviolet photolysis of ICN in organic solvents. J. Phys. Chem. A **119**, 12911 (2015)

65. P. Hamm, Coherent effects in femtosecond infrared spectroscopy. Chem. Phys. **200**, 415 (1995)